

# Collapse of Axion Domain Wall Induced by Helical Primordial Magnetic Fields

Zizhuo Zhao,<sup>1,2</sup> Yuefeng Di,<sup>3,4</sup> Ligong Bian,<sup>5,\*</sup> and Jing Shu<sup>6,7,8,†</sup>

<sup>1</sup> *University of Chinese Academy of Sciences (UCAS), Beijing 100049, P.R. China*

<sup>2</sup> *International Center for Theoretical Physics Asia-Pacific, Beijing/Hangzhou, P.R. China*

<sup>3</sup> *Institute of Theoretical Physics, Chinese Academy of Sciences, Beijing 100190, China*

<sup>4</sup> *School of Physical Sciences, University of Chinese Academy of Sciences (UCAS), Beijing 100049, China*

<sup>5</sup> *Department of Physics and Chongqing Key Laboratory for Strongly Coupled Physics,*

*Chongqing University, Chongqing 401331, P. R. China*

<sup>6</sup> *School of Physics and State Key Laboratory of Nuclear Physics and Technology, Peking University, Beijing 100871, China*

<sup>7</sup> *Center for High Energy Physics, Peking University, Beijing 100871, China*

<sup>8</sup> *Beijing Laser Acceleration Innovation Center, Huairou, Beijing, 101400, China*

Stable domain wall (DW) must decay to avoid overclose the Universe. A commonly used solution is to slightly break the PQ symmetry by introducing a bias term in the potential. In this work, we propose an alternative, symmetry-preserving mechanism: coupling the axion field to a helical primordial magnetic field (PMF) via the Chern–Simons term. Using three-dimensional lattice simulations, we evolve the DW network and demonstrate that it can successfully drive DW decay. Our quantitative results further show that the correlation length of the PMF plays a crucial role in determining the decay rate of the DW network and the resulting axion and gravitational wave radiation.

**Introduction.** The QCD axion, as a pseudo–Nambu–Goldstone boson associated with the spontaneous breaking of the Peccei–Quinn (PQ) symmetry, was originally proposed to solve the strong CP problem [1–4] and is also a compelling dark matter (DM) candidate [5, 6]. The breaking of PQ symmetry produces cosmic strings, and the QCD axion field acquires a potential at the QCD scale, leading to the formation of domain walls (DWs) attached to the strings [7]. The number of walls attached to a single string is defined as the domain wall number  $N_{DW}$ . For  $N_{DW} = 1$ , the DW network is unstable and decays rapidly, whereas for  $N_{DW} > 1$  they become stable and can eventually dominate the cosmic energy density, leading to the cosmological domain wall problem [8, 9]. Various solutions have been proposed, such as introducing a bias term between different vacua in the potential [10–13], the Lazarides–Shafi (LS) mechanism [14–16] and introducing a light axion-like particle (ALP) coupled to gluons [17].

Previous lattice studies have simulated QCD-axion DWs without gauge couplings [18–21], and works that include gauge couplings have primarily provided analytical analysis of friction effects [22]. However, simulating the coupling between DW networks and gauge fields is necessary due to the experimental significance of axion-gauge field interactions [23]. We address this gap by simulating the QCD axion field couples through Chern-Simons (CS) term with the primordial magnetic field (PMF), which is considered as seed of magnetic field in the Universe and can be generated in the early Universe (e.g., around the QCD phase transition [24] or during inflation [25–28]). The origin of PMF determines their correlation length, and in some scenarios they may also carry nonzero helicity.

In this Letter, we perform the first large-scale three-dimensional lattice simulations of axion DWs coupled to

a  $U(1)$  gauge field. We propose a novel mechanism in which gauge coupling induces the decay of stable DW networks, providing a new decay channel that does not rely on an additional bias term or ALPs. Previous work [29] studied axion production from a spatially uniform axion field coupled to a helical PMF using analytical methods. Here, we investigate in detail how the correlation length of a helical PMF affects the decay rate of DW networks, as well as the resulting axion and gravitational wave (GW) radiation. Using our results, we derive constraints on the PQ scale or axion decay constant  $f_a$  and on the PMF correlation length  $\lambda_B$  from the axion energy density, and we obtain a potentially detectable GW spectrum.

**The simulation setup.** We consider an axion model coupling with the gauge field through the CS term  $F_{\mu\nu}\tilde{F}^{\mu\nu}$ . Using conformal time  $\tau$  and the FLRW metric  $g_{\mu\nu} = a^2(\tau)(-d\tau^2 + dx^2)$ , the action is

$$S = \int d^4x \sqrt{-g} \left[ -\partial_\mu \phi \partial^\mu \phi - \frac{1}{4} F_{\mu\nu} F^{\mu\nu} - V(\phi) - \alpha \frac{\phi}{v} F_{\mu\nu} \tilde{F}^{\mu\nu} \right] \quad (1)$$

where  $\phi$  is axion field and  $\alpha$  is dimensionless coupling constant. The parameter  $v$  is the PQ vacuum and the ratio  $\theta = \frac{\phi}{v}$  can be seen as the phase of PQ field. The field strength tensor and its dual tensor are defined by  $F_{\mu\nu} = \partial_\mu A_\nu - \partial_\nu A_\mu$ ,  $\tilde{F}_{\mu\nu} = \frac{1}{2} \epsilon_{\mu\nu\rho\sigma} F^{\rho\sigma}$ , where  $\epsilon_{\mu\nu\rho\sigma}$  is Levi-Civita symbol and  $\epsilon_{0123} = 1$ . We use the potential

$$V(\phi) = \frac{m_a(T)^2 v^2}{N_{DW}^2} \left( 1 - \cos \left( N_{DW} \frac{\phi}{v} \right) \right) \quad (2)$$

When temperature  $T > 100\text{MeV}$ , the axion mass  $m_a(T)$  can be parametrized as [30]

$$m_a(T)^2 = \frac{\alpha_a \Lambda^4}{f_a^2 (T/\Lambda)^{6.68}} \quad (3)$$

where  $\alpha_a = 1.68 \times 10^{-7}$ ,  $\Lambda = 400$  MeV and  $f_a = v/N_{DW}$ . When  $T \leq 100$  MeV, the axion mass no longer grows and is substituted by a zero-temperature mass  $m_{a,0} = 5.707 \times 10^{-5} (10^{11} \text{ GeV}/f_a) \text{ eV}$  [31].

This potential has  $N_{DW}$  degenerate minima, corresponding to  $N_{DW}$  distinct vacua. During the phase transition, the axion field settles into different vacua in different regions, and the boundaries between these regions after the transition form DWs. The width and tension of these DWs are  $r_{dw} \sim m_a^{-1}$ ,  $\sigma_{dw} \sim m_a f_a^2$  [7]. The oscillation of DWs can be the source of GW and the energy density of GW can be calculated by  $\rho_{gw} \sim G\sigma_{dw}^2$  [32]. The DWs always evolve to scaling regime [7], when the DW area per Hubble patch  $\mathcal{A}$  is a constant. But some deviations appear in some researches [19, 33]. With the total area of DWs  $A$  and the total volume  $V$ , we define  $\mathcal{A}$  as the scaling parameter

$$\mathcal{A} = \frac{At}{V} \quad (4)$$

In our code, we use the same method as [20] to identify the location of DWs.

Adopting the temporal gauge  $A_0 = 0$ , the equations of motion (EOM) are [34, 35]

$$\begin{aligned} \phi'' &= \partial_i \partial_i \phi - 2\mathcal{H}\phi' - a^2 \frac{dV}{d\phi} - a^2 \frac{\alpha}{4v} F_{\mu\nu} \tilde{F}^{\mu\nu} \\ E'_i &= -\epsilon_{ijk} \partial_j B_k + \frac{\alpha}{v} \phi' B_i - \frac{\alpha}{v} \epsilon_{ijk} \partial_j \phi E_k \\ \partial_i A'_i &= \frac{\alpha}{v} \partial_i \phi \epsilon_{ijk} \partial_j A_k \end{aligned} \quad (5)$$

where  $\phi' = \partial\phi/\partial\tau$  and  $A_i$  is comoving gauge field. In addition,  $E_i = \frac{1}{a^2} A'_i$  and  $B_i = \frac{1}{a^2} \epsilon_{ijk} \partial_j A_k$  are the physical electric and magnetic field and  $\mathcal{H} = aH$  is conformal Hubble. The third equation is the Gauss constraint, arising naturally from gauge invariance. The CS term  $F_{\mu\nu} \tilde{F}^{\mu\nu}$  can be written by

$$F_{\mu\nu} \tilde{F}^{\mu\nu} = 4 \sum_i E_i B_i \quad (6)$$

We use the discretization scheme mentioned in [34] to evolve the above equations on the lattice.

In this work, we consider the PMF with finite correlation length  $\lambda_B$  and helicity  $\mathcal{H}$ , which are defined by

$$\lambda_B = \frac{\int dk E_B(k)/k}{\int dk E_B(k)}, \quad \mathcal{H} = \int dx^3 \mathbf{A} \cdot \mathbf{B}_c \quad (7)$$

where  $\int dk E_B(k) = \frac{1}{2V} \int d^3x |\vec{B}(x)|^2$  is the magnetic field energy density and  $\mathbf{B}_c = \nabla \times \mathbf{A}$  is the comoving magnetic field. The time derivative of helicity determines the average CS term [36]

$$\frac{d\mathcal{H}}{d\tau} = -2 \int dx^3 \mathbf{E}_c \cdot \mathbf{B}_c \quad (8)$$

where  $\mathbf{E}_c = \mathbf{A}'$  is comoving electric field. From the axion EOM in Eq. 5, the effective potential

$$V_{eff}(\phi) = V(\phi) + \frac{\alpha}{4v} \phi F_{\mu\nu} \tilde{F}^{\mu\nu} = V(\phi) + \Delta V(\phi) \quad (9)$$

is tilted by the CS coupling term  $\Delta V(\phi)$ , which selects a preferred vacuum of  $V(\phi)$  and drives the axion field toward it. However, if the spatial average of the CS term vanishes, the sign of  $F_{\mu\nu} \tilde{F}^{\mu\nu}$  — and hence the preferred vacuum — differs from site to site, resulting in a cancellation of the driving force. This corresponds to the case of constant helicity. In contrast, a nonzero averaged CS term, corresponding an oscillating helicity, selects a unique vacuum of  $V(\phi)$  and inducing a net drift of the axion field, reflected in a nonzero  $\langle\phi'\rangle$  that leads to DW-network decay. Because the physical CS term is suppressed as  $a^{-4}$ , the tilt of  $V_{eff}$  — and hence the induced average velocity — arises mainly at early times, before the DW network forms. Although the CS term becomes negligible later and cannot further accelerate the field, the previously generated average velocity persists and eventually drives the collapse of the DW network.

The GW is generated through oscillations of DWs. In lattice simulations, the evolution of the metric perturbation  $h_{ij}$  is governed by

$$h''_{ij} - \nabla^2 h_{ij} + 2\mathcal{H}h'_{ij} = 16\pi G T_{ij}^{TT}, \quad (10)$$

where  $T_{ij}^{TT}$  is the transverse-traceless component of the energy-momentum tensor, defined as [35]:

$$T_{ij}^{TT} = \partial_i \phi \partial_j \phi + F_{i\alpha} F_{\beta j} g^{\alpha\beta} \quad (11)$$

with  $g_{\mu\nu}$  being the FLRW metric. The dimensionless GW spectrum is then calculated by:

$$\Omega_{gw}(k) = \frac{1}{\rho_c} \frac{\partial \rho_{gw}(k)}{\partial \ln k} = \frac{1}{24\pi^2 V} \frac{k^3}{\mathcal{H}^2} \sum_{ij} |h'_{ij}(k, \tau)|^2, \quad (12)$$

where  $h_{ij}(k, \tau)$  denotes the Fourier transform of  $h_{ij}(x)$ ,  $V$  is the comoving volume of the whole lattice and  $\rho_c = 3/(8\pi G)H^2$  is the critical energy density. When calculating GW spectrum from the lattice simulation, we use the Runge-Kutta method to numerically solve Eq.(10), and the calculation of the GW spectrum within the lattice simulation is performed using the Pystella code introduced in [35].

We simulate the evolution during the QCD phase transition. The initial temperature is set to  $T_i = 220 \text{ MeV}$ , and the PQ vacuum is taken as  $v = N_{DW} f_a$ , with  $N_{DW} = 3$  and  $f_a = 1.8 \times 10^{16} \text{ GeV}$ . The effective degrees of freedom  $g(T)$ , scale factor  $a(T)$ , and Hubble parameter  $H(T)$  are determined using the expressions provided in [20]. In the simulation, we set  $f_* = v$  and  $w_* = 6a_i H_i$ ,  $a_i$  and  $H_i$  denote the initial values of  $a(T)$  and  $H(T)$ , to define dimensionless varieties

$$\phi = \frac{\phi}{f_*}, \quad \tilde{A}_i = \frac{A_i}{w_*}, \quad \tilde{x} = w_* x, \quad \tau = w_* \tau \quad (13)$$

We use the rescaled conformal time  $\tau = \tau/\tau_i$  to show our results, with the initial conformal time  $\tau_i = 1/(a_i H_i)$ . We use a lattice of size  $N^3 = 1024^3$ , corresponding to an initial volume that contains  $10.24^3$  Hubble volumes. The dimensionless spatial and temporal intervals are set to  $d\tilde{x} = 0.06$  and  $d\tau = 0.01$ , ensuring that the physical spatial interval  $dx$  remains smaller than the DW width  $r_{dw}$  throughout the entire evolution.

For the PMF with finite correlation length, it is defined in the momentum space [37]

$$B_i(\vec{k}) = B_{ini} \Theta(k - k_{UV}) (\delta_{ij} - \hat{k}_i \hat{k}_j - i \sigma_M \epsilon_{ijl} \hat{k}_l) g_j(\vec{k}) k^n \quad (14)$$

where  $k_{UV}$  is the cutoff for the primordial magnetic field and  $g_j(\vec{k})$  is the Fourier transform of a Gaussian distributed random vector field that is  $\delta$ -correlated in all three dimensions. The power  $n$  is spectrum index and  $\sigma_M \in [-1, 1]$  determines the helicity.

$$f_H = \frac{\sum_k h(k)}{\sum_k \frac{2\rho_B(k)}{k}} = \frac{2\sigma_M}{1 + \sigma_M^2} \quad (15)$$

where  $h(k)$  and  $\rho_B(k)$  denote the helicity and energy density of the magnetic field in momentum space, respectively. This relation indicates that for a fixed magnetic energy density, the helicity is determined solely by the parameter  $\sigma_M$ . The detailed derivation is provided in the Supplemental Material. The spectrum index of the initial magnetic field is fixed at  $n = 2$ . The initial value of PQ phase  $\theta$  is set as a uniform random distribution between 0 and  $2\pi$ . The detailed analysis of initial axion and gauge field is shown in the Supplemental Material.

Here, we note that, for the fixed energy density of the PMF, the CS term satisfies  $F_{\mu\nu} \tilde{F}^{\mu\nu} \propto f_H$ . In addition, when the CS term is fixed, the effect of the coupling constant  $\alpha$  appears solely through the coupling term, meaning that the influence of  $\alpha$  follows the same scaling behavior as  $f_H$  as will be explored latter. In this work, we simulate the case without CS term by set  $\alpha = 0$ , and using  $\alpha = 0.2$  to consider the case with the CS term.

**Numerical results.** We first present the evolution of the scaling parameter in Fig. 1. The top panel shows the results for different correlation lengths. For  $\alpha = 0$ , the DW network remains approximately in the scaling regime, whereas the decrease of  $\mathcal{A}$  in the other cases signals the decay of DWs. As discussed above, the decay rate is governed by the average CS term, which is shown in the Supplemental Material. For short correlation lengths, the average CS term exhibits rapid oscillations, which partially cancel the average velocity of the axion field generated during the positive and negative phases of the CS term. Consequently, the DWs decay more slowly when the correlation length is small. In contrast, for cases with long correlation lengths, the average CS term decreases as the correlation length increases, since the helicity oscillates more slowly. The small average CS term reduces the net velocity of the axion field,

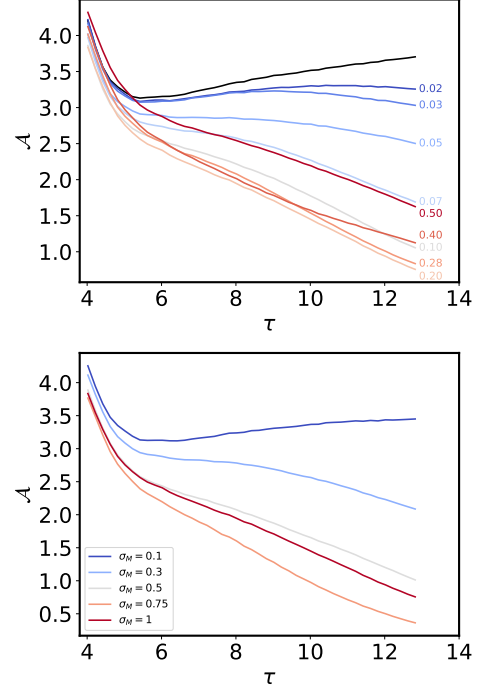


Figure 1: The results of scaling parameter  $\mathcal{A}$ . The top panel shows the cases with the fixed  $\sigma_M = 1$ . The value at the tail of each curve in the first figure indicates the corresponding  $\lambda_B H_i$  associated with that case. The black curve corresponds the case  $\alpha = 0$ . The bottom panel shows the cases the fixed  $\lambda_B \sim 0.2 H_i^{-1}$ .

thereby slowing down the decay of DWs. Considering both the magnitude and the oscillation rate of the average CS term, the DWs decay most rapidly at an intermediate, optimal correlation length. We further note that the physical CS term is suppressed by  $a^{-4}$ , so it is only at early times that this term is sufficiently large to significantly influence the evolution of the axion field.

The bottom panel of Fig.1 displays the scaling parameter for the case  $\lambda_B \sim 0.2 H_i^{-1}$  with different values of  $\sigma_M$ . From Eq.8 and Eq. 15,  $\sigma_M$  determines the ratio  $f_H$  and thus sets the helicity amplitude for magnetic fields with fixed energy density. As a result,  $\sigma_M$  also controls the strength of the average CS term. Accordingly, the DW network decays more slowly for smaller  $\sigma_M$ . Notably, when  $\sigma_M = 0.1$ , the scaling parameter  $\mathcal{A}$  evolves in nearly the same manner as in the no-coupling case, indicating that the helicity is too weak to affect the DW network evolution; therefore, we exclude this case from the subsequent discussion.

We suppose the decrease of scaling parameter  $\mathcal{A}$  satisfies

$$\mathcal{A}(t) = \mathcal{A}_{\text{form}} \left( \frac{t}{t_{\text{form}}} \right)^{1-p} \quad (16)$$

where we choose the DWs form with the scaling param-

ter  $\mathcal{A}_{\text{form}}$  at time  $t_{\text{form}}$ . For the case  $\alpha = 0$ , the parameter  $p$  is constant and slightly smaller than 1, showing the deviation from the scaling regime [19]. While for  $\alpha \neq 0$ ,  $p$  exhibits a linear increase with time, as shown in the Supplemental Material. We perform a linear fit to obtain the function  $p(t)$ , which is then substituted into the equation to extrapolate the long-time evolution of  $\mathcal{A}$  and determine the decay time of the DW network. We define the DW network as completely collapsed when the scaling parameter  $\mathcal{A}$  decreases to  $0.01\mathcal{A}_{\text{form}}$  or  $0.1\mathcal{A}_{\text{form}}$ . The corresponding decay times for different  $\lambda_B$  cases are shown in the Supplemental Material. Both criteria indicate that the relationship between the decay time  $\log_{10}(\frac{t_{\text{dec}}}{t_{\text{form}}})$  and the correlation length  $\log_{10}(\lambda_B H_i)$  is piecewise linear, from which we can also derive the corresponding fitting function. This piecewise linear behavior reflects the presence of different dominant factors in the long- and short-correlation regimes as discussed above.

In addition, we also present the results of  $\log_{10}(\frac{t_{\text{dec}}}{t_{\text{form}}})$  for different values of  $\sigma_M$  with a fixed  $\lambda_B \sim 0.2H_i^{-1}$  in the Supplemental Material. For all considered  $\sigma_M$ , the parameter  $p$  still exhibits a linear increase with time, allowing us to calculate the decay time as before. These results are well described by  $\log_{10}(\frac{t_{\text{dec}}}{t_{\text{form}}}) \propto 1/f_H = \frac{1+\sigma_M^2}{2\sigma_M}$ , indicating that the decay rate increases exponentially with  $f_H$ , and hence grows exponentially with the helicity magnitude.

The DW network can radiate its energy into free axion. In the pure axion case, the network nearly reaches a scaling regime, so most of the energy cannot be emitted as free axion, and the axion energy is related to the parameter  $p$  [19]. However, when gauge coupling is taken into account, the DWs decay rapidly, and we assume that the entire energy of the DW network is converted into free axion. Using the derivation in the Supplemental Material, we obtain the present-day energy density ratio between axion and dark matter for the gauge-coupling cases,  $\Omega_a/\Omega_{DM}$ , as given in the first line of Eq. 17.

To obtain these results, we require the average momentum parameter  $\epsilon_a = \bar{k}/m_a$ , where  $\bar{k} = \frac{\int \rho_a(k) dk}{\int (\rho_a(k)/k) dk}$  is the average momentum, and the scaling parameter at the time of DW network formation,  $\mathcal{A}_{\text{form}}$ , for each case. These results are presented in the Supplemental Material. For cases with fixed  $\sigma_M = 1$ , a piecewise linear relationship is again observed between  $\mathcal{A}_{\text{form}}$  and  $\log_{10}(\lambda_B H_i)$ . This behavior arises because, when the net velocity of the axion field is too large, the field rapidly relaxes to its preferred vacuum, leading to a smaller DW area. The parameter  $\epsilon_a$  decreases over time and approaches a constant value. Its average over the final few time steps shows a clear linear increase with the correlation length,  $\log_{10}(\lambda_B H_i)$ . The factors  $\epsilon_a$ ,  $\mathcal{A}$  and  $\frac{t_{\text{dec}}}{t_{\text{form}}}$  can now be fitted as functions of the correlation length  $\lambda_B$ . The momentum parameter in our simulations,  $\epsilon_a \sim 0.5$ –1, is smaller than the value  $\epsilon_a \sim 1.2$  reported in Ref.[19], while

our scaling parameter at formation,  $\mathcal{A}_{\text{form}} \sim 3$ , is larger than their reported value  $\mathcal{A} \sim 0.8$  for  $N_{DW} = 3$ . Moreover, Ref.[19] assumes that the DW network remains in a scaling regime, whereas in our simulations the network radiates continuously. We therefore assume that the entire DW energy density at formation is converted into axion, resulting in a larger axion emission than that obtained in Ref.[19]. Additionally, we present results for different  $\sigma_M$  with fixed  $\lambda_B \sim 0.2H_i^{-1}$  in the Supplemental Material, which follow  $\mathcal{A}_{\text{form}} \propto 1/f_H$  and  $\epsilon_a \propto f_H$ .

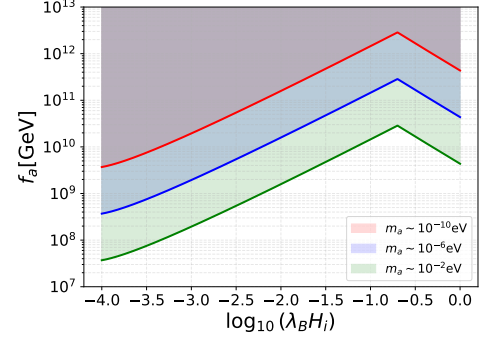


Figure 2: The parameter space of  $f_a$  and  $\lambda_B$ . We choose  $C = C_0$  and different  $m_a$ . The shaded region represents the forbidden region  $\Omega_a > \Omega_{DM}$ .

With the analysis in the Supplemental Material, we can get the results of relic density of the axion:

$$\frac{\Omega_a}{\Omega_{DM}} \sim 0.085 \epsilon_a \mathcal{A}_{\text{form}} \left( \frac{t_{\text{dec}}}{t_{\text{form}}} \right)^{3/2} \left( \frac{10.75}{g_*(T_{\text{dec}})} \right)^{1/4} \times \left( \frac{f_a}{10^{12} \text{GeV}} \right)^2 \left( \frac{m_a}{10^{-6} \text{eV}} \right)^{1/2}, \quad (17)$$

wherein, relevant parameters are given by,

$$\begin{aligned} \epsilon_a &= 0.19x + 0.82 + 0.18 \left( \frac{C}{C_0} - 1 \right) \\ \mathcal{A}_{\text{form}} &= 0.49 \left( \frac{C_0}{C} - 1 \right) + \begin{cases} -0.48x + 2.38, & x < -0.7 \\ 1.15x + 3.52, & x \geq -0.7 \end{cases} \\ \log_{10} \left( \frac{t_{\text{dec}}}{t_{\text{form}}} \right) &= 0.78 \left( \frac{C_0}{C} - 1 \right) + \begin{cases} -1.34x + 0.07, & x < -0.7 \\ 1.38x + 1.97, & x \geq -0.7 \end{cases} \end{aligned} \quad (18)$$

with  $x = \log_{10}(\lambda_B H_i)$ . The parameter  $C$  is the coupling term, defined as

$$C = C(\alpha, B_{\text{ini}}, f_H) = \left( \frac{\alpha}{\alpha_0} \right) \left( \frac{B_{\text{ini}}^2}{B_0^2} \right) \left( \frac{f_H}{f_{H,0}} \right) C_0 \quad (19)$$

$\alpha_0 = 0.2$ ,  $f_{H,0} = 1$  are the reference values adopted in our simulations.  $C_0$  is then the coupling term when choosing  $\alpha = \alpha_0$ ,  $B_{\text{ini}} = B_0$ ,  $f_H = f_{H,0}$ . In the second line

of Eq.17, we use the same normalization parameters as paper [38]. Using the constraint  $\Omega_a/\Omega_{\text{DM}} \leq 1$ , we then obtain the allowed parameter space of  $\lambda_B$  and  $f_a$  for a given axion mass  $m_a$ , which is presented in Fig. 2.

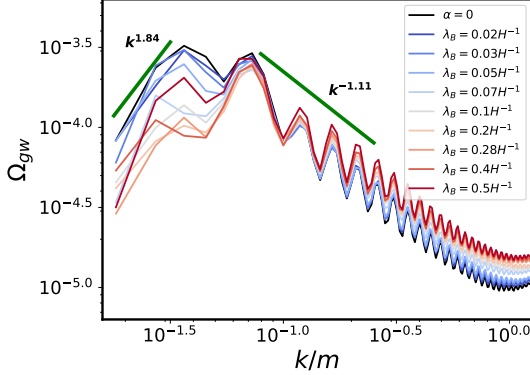


Figure 3: The GW spectra at  $\tau = 11$  are shown. The unphysical high-frequency region corresponding to scales smaller than the DW width (with  $k > m$ ) has been removed.

Next we consider the GW radiation of DW network. We first present the GW spectra radiated at  $\tau = 11$  for each case in the Fig. 3. The low-frequency part of the spectra is small for fast-decay cases, which is because the decay of DWs reduces the GW source, particularly at large scales. In addition, we find that the peak value of the GW spectra grows approximately as  $H^{-2}(\tau)$ , consistent with the results of [32]. Using  $\rho_{gw} \sim G\sigma_{dw}^2 \sim Gf_a^4 m_a^2$ , the peak value can be parameterized as  $\Omega_{gw}^p(\tau) \propto H^{-2}(\tau)f_a^4 m_a^2$ . Although the GW energy density also depends on  $\mathcal{A}$ , since the DW energy density itself scales with  $\mathcal{A}$ , we absorb this dependence into an overall coefficient. This is because the relevant value of  $\mathcal{A}$  is the one at the time of GW emission rather than at the formation of the DW network. As the DW network is not in the scaling regime and  $\mathcal{A}$  evolves significantly during the network's lifetime, its instantaneous value is highly time-dependent and thus not a meaningful standalone parameter. Instead, its effect is fully encoded in the evolution of the network and therefore incorporated into the fitted coefficient. With the calculation shown in the Supplemental Material, we obtain the strength of the spectrum at the peak in the first line of Eq. 20, which is redshifted to the present epoch:

$$\Omega_{gw,0}^p = \tilde{\Omega} \left( \frac{t_{\text{dec}}}{t_{\text{form}}} \right)^2 \left( \frac{f_a}{1.8 \times 10^{16} \text{GeV}} \right)^4 \left( \frac{10.75}{g_*(T_{\text{dec}})} \right)^{4/3} \quad (20)$$

where the factor  $\tilde{\Omega}$  is of the piecewise linear function:

$$\tilde{\Omega} = 10^{-14} \left( 1.33 \left( \frac{C_0}{C} - 1 \right) + \begin{cases} -1.71x + 3.2, & x < -0.7 \\ 2.01x + 5.8, & x \geq -0.7 \end{cases} \right)$$

where  $x = \log_{10}(\lambda_B H_i)$ . We compute the GW efficiency parameter  $\epsilon_{gw} = \rho_{gw}/(G\sigma_{dw}^2)$ , finding that it is approximately an order of magnitude smaller than the value reported in Ref. [18], but it is close to the results presented in Ref.[32]. We also investigate the effect of  $\sigma_M$  on GW emission for the case  $\lambda_B \sim 0.2H_i^{-1}$ , as presented in the Supplemental Material. The results show that  $\Omega_{gw,0}^p h^2 \propto 1/f_H$ , which is consistent with the expectation that a faster-decaying DW network produces weaker GW radiation. Using the peak value of the GW spectrum and the spectral slopes on both sides of the peak, we can determine the GW spectrum emitted at the time of DW network collapse and observed today, as shown in Fig. 4. Wherein, we can find that the predicted GW spectra could be detected by PTA experiments and LISA in the near future. The GW reported by us would DW explanation of the signature of the stochastic GW background reported by PTA experiments (such as: NanoGrav, PPTA, EPTA, and CPTA),

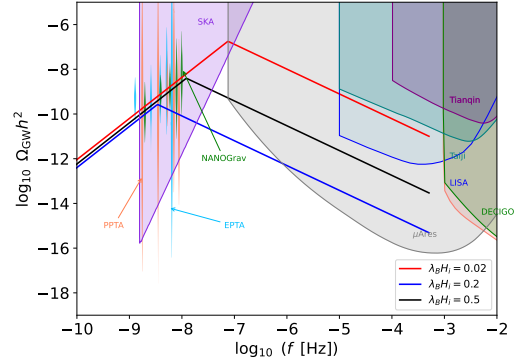


Figure 4: Detectability of the GW spectra for  $\lambda_B$  cases. We use  $f_a = 5 \times 10^{16} \text{GeV}$ . The sensitivity curves of LISA [39, 40], TianQin [41, 42], Taiji [43, 44],  $\mu\text{Ares}$  [45], DECIGO [46–49], BBO [50–52], SKA [53], NANOGrav [54], PPTA [55] and EPTA [56] are presented.

**Conclusion and Discussion.** We have performed three-dimensional lattice simulations of axion DW networks coupled to a PMF via the CS term during the QCD epoch. Our results reveal a novel decay channel for stable DW networks ( $N_{\text{DW}} = 1$ ): oscillations of the magnetic helicity, i.e., a nonzero average  $\langle F\tilde{F} \rangle \propto \langle \mathbf{E} \cdot \mathbf{B} \rangle$ , imparting a net drift velocity to the axion field. This velocity selects a preferred vacuum and triggers DW collapse without an explicit bias term. The decay rate depends sensitively on the PMF correlation length  $\lambda_B$  and helicity strength. Short-correlation PMFs produce near-cancellation of the axion velocity due to rapid CS-term oscillations, while long-correlation PMFs yield a small net CS term because of slow helicity oscillations; both effects slow DW decay. From the fitted decay time dependence on  $\lambda_B$ , we deter-

mine axion radiation as a function of  $\lambda_B$ , constraining both  $f_a$  and  $\lambda_B$ . We further present GW spectra for different  $\lambda_B$  and derive the corresponding GW radiation, providing correlated predictions for axion dark matter and GW signals as clear targets for future observations, such as PTA experiments.

**Acknowledgments.** This work is supported by the National Key Research and Development Program of China under Grant No.2021YFC2203004, and by the National Natural Science Foundation of China (NSFC) under Grants Nos.2322505, 12347101. We also acknowledges Chongqing Talents: Exceptional Young Talents Project No. cstc2024ycjhbzxm0020 and Chongqing Natural Science Foundation under Grant No. CSTB2024NSCQJQX0022. J.S. is supported by the Peking University under startup Grant No.7101302974, the NSFC under Grants No.12025507, No.12450006.

---

\* lgbycl@cqu.edu.cn

† jshu@pku.edu.cn

- [1] R. D. Peccei and H. R. Quinn, Phys. Rev. Lett. **38**, 1440 (1977).
- [2] R. D. Peccei and H. R. Quinn, Phys. Rev. D **16**, 1791 (1977).
- [3] S. Weinberg, Phys. Rev. Lett. **40**, 223 (1978).
- [4] F. Wilczek, Phys. Rev. Lett. **40**, 279 (1978).
- [5] L. Di Luzio, M. Giannotti, E. Nardi, and L. Visinelli, Physics Reports **870**, 1–117 (2020).
- [6] C. O’Hare, in *Proceedings of 1st General Meeting and 1st Training School of the COST Action COSMIC WISIPers — PoS(COSMICWISIPers)*, COSMICWISIPers (Sissa Medialab, 2024) p. 040.
- [7] A. Vilenkin and E. P. S. Shellard, *Cosmic Strings and Other Topological Defects* (Cambridge University Press, 2000).
- [8] Y. B. Zeldovich, I. Y. Kobzarev, and L. B. Okun, Zh. Eksp. Teor. Fiz. **67**, 3 (1974).
- [9] P. Sikivie, Phys. Rev. Lett. **48**, 1156 (1982).
- [10] G. B. Gelmini, M. Gleiser, and E. W. Kolb, Phys. Rev. D **39**, 1558 (1989).
- [11] S. E. Larsson, S. Sarkar, and P. L. White, Physical Review D **55**, 5129–5135 (1997).
- [12] M. Kamionkowski and J. March-Russell, Physics Letters B **282**, 137–141 (1992).
- [13] S. M. Barr and D. Seckel, Phys. Rev. D **46**, 539 (1992).
- [14] G. Lazarides and Q. Shafi, Physics Letters B **115**, 21 (1982).
- [15] R. Sato, F. Takahashi, and M. Yamada, Physical Review D **98** (2018), 10.1103/physrevd.98.043535.
- [16] C. Chatterjee, T. Higaki, and M. Nitta, Physical Review D **101** (2020), 10.1103/physrevd.101.075026.
- [17] J. Lee, K. Murai, F. Takahashi, and W. Yin, “Resolving the qcd axion domain wall problem with a light axion,” (2025), arXiv:2507.07075 [hep-ph].
- [18] T. Hiramatsu, M. Kawasaki, K. Saikawa, and T. Sekiguchi, Journal of Cosmology and Astroparticle Physics **2013**, 001–001 (2013).
- [19] M. Kawasaki, K. Saikawa, and T. Sekiguchi, Physical Review D **91** (2015), 10.1103/physrevd.91.065014.
- [20] Y. Li, L. Bian, R.-G. Cai, and J. Shu, “Cosmic simulations of axion string-wall networks: Probing dark matter and gravitational waves for discovery,” (2024), arXiv:2311.02011 [astro-ph.CO].
- [21] Y.-J. Li, J. Liu, and Z.-K. Guo, “Dynamics of  $z_n$  domain walls with bias directions,” (2025), arXiv:2502.13644 [astro-ph.CO].
- [22] S. Hassan, G. R. Kane, J. March-Russell, and G. Obied, “Chern-simons induced thermal friction on axion domain walls,” (2024), arXiv:2410.19906 [hep-ph].
- [23] G. Carosi, A. Friedland, M. Giannotti, M. J. Pivovarov, J. Ruz, and J. K. Vogel, “Probing the axion-photon coupling: phenomenological and experimental perspectives. a snowmass white paper,” (2013), arXiv:1309.7035 [hep-ph].
- [24] T. Vachaspati, Physics Letters B **265**, 258 (1991).
- [25] P. Adshead, J. T. Giblin, T. R. Scully, and E. I. Sfakianakis, Journal of Cosmology and Astroparticle Physics **2016**, 039–039 (2016).
- [26] M. S. Turner and L. M. Widrow, Phys. Rev. D **37**, 2743 (1988).
- [27] J. Martin and J. Yokoyama, Journal of Cosmology and Astroparticle Physics **2008**, 025 (2008).
- [28] S. Kanno, J. Soda, and M.-a. Watanabe, Journal of Cosmology and Astroparticle Physics **2009**, 009–009 (2009).
- [29] L. Campanelli and M. Giannotti, Phys. Rev. Lett. **96**, 161302 (2006).
- [30] O. Wantz and E. P. S. Shellard, Physical Review D **82** (2010), 10.1103/physrevd.82.123508.
- [31] G. G. di Cortona, E. Hardy, J. P. Vega, and G. Villadoro, Journal of High Energy Physics **2016** (2016), 10.1007/jhep01(2016)034.
- [32] I. Dankovsky, E. Babichev, D. Gorbunov, S. Ramazanov, and A. Vikman, Journal of Cosmology and Astroparticle Physics **2024**, 047 (2024).
- [33] K. S. Jeong, M. Kawasaki, and F. Takahashi, Journal of Cosmology and Astroparticle Physics **2014**, 046–046 (2014).
- [34] D. G. Figueroa and M. Shaposhnikov, Nuclear Physics B **926**, 544–569 (2018).
- [35] P. Adshead, J. T. Giblin, M. Pieroni, and Z. J. Weiner, Physical Review Letters **124** (2020), 10.1103/physrevlett.124.171301.
- [36] L. Campanelli and M. Giannotti, Phys. Rev. D **72**, 123001 (2005).
- [37] A. Brandenburg, R. Durrer, Y. Huang, T. Kahniashvili, S. Mandal, and S. Mukohyama, Phys. Rev. D **102**, 023536 (2020).
- [38] M. Gorghetto and E. Hardy, Journal of High Energy Physics **2023** (2023), 10.1007/jhep05(2023)030.
- [39] P. A.-S. et al., “Laser interferometer space antenna,” (2017), arXiv:1702.00786 [astro-ph.IM].
- [40] J. B. et al., “The laser interferometer space antenna: Unveiling the millihertz gravitational wave sky,” (2019), arXiv:1907.06482 [astro-ph.IM].
- [41] J. e. a. Luo, Classical and Quantum Gravity **33**, 035010 (2016).
- [42] K. Zhou, J. Cheng, and L. Ren, “Detecting anisotropies of the stochastic gravitational wave background with tianqin,” (2023), arXiv:2306.14439 [gr-qc].
- [43] W.-R. Hu and Y.-L. Wu, National Science Review **4**, 685 (2017), <https://academic.oup.com/nsr/article-pdf/4/5/685/31566708/nwx116.pdf>.

- [44] W.-H. Ruan, Z.-K. Guo, R.-G. Cai, and Y.-Z. Zhang, *International Journal of Modern Physics A* **35**, 2050075 (2020).
- [45] A. e. a. Sesana, *Experimental Astronomy* **51**, 1333–1383 (2021).
- [46] N. Seto, S. Kawamura, and T. Nakamura, *Physical Review Letters* **87** (2001), 10.1103/physrevlett.87.221103.
- [47] S. e. a. Kawamura, *Classical and Quantum Gravity* **28**, 094011 (2011).
- [48] K. Yagi and N. Seto, *Physical Review D* **83** (2011), 10.1103/physrevd.83.044011.
- [49] S. Isoyama, H. Nakano, and T. Nakamura, *Progress of Theoretical and Experimental Physics* **2018** (2018), 10.1093/ptep/pty078.
- [50] J. Crowder and N. J. Cornish, *Physical Review D* **72** (2005), 10.1103/physrevd.72.083005.
- [51] V. Corbin and N. J. Cornish, *Classical and Quantum Gravity* **23**, 2435–2446 (2006).
- [52] G. M. Harry, P. Fritschel, D. A. Shaddock, W. Folkner, and E. S. Phinney, *Classical and Quantum Gravity* **23**, 4887 (2006).
- [53] G. H. Janssen, G. Hobbs, M. McLaughlin, C. G. Bassa, A. T. Deller, M. Kramer, K. J. Lee, C. M. F. Mingarelli, P. A. Rosado, S. Sanidas, A. Sesana, L. Shao, I. H. Stairs, B. W. Stappers, and J. P. W. Verbiest, “Gravitational wave astronomy with the ska,” (2014), arXiv:1501.00127 [astro-ph.IM].
- [54] Z. e. a. Arzoumanian, *The Astrophysical Journal Letters* **905**, L34 (2020).
- [55] B. e. a. Goncharov, *The Astrophysical Journal Letters* **917**, L19 (2021).
- [56] S. e. a. Chen, *Monthly Notices of the Royal Astronomical Society* **508**, 4970–4993 (2021).
- [57] Y. Di, L. Bian, and R.-G. Cai, “Magnetic field effects on electroweak phase transition and baryon asymmetry,” (2024), arXiv:2409.16124 [hep-ph].
- [58] T. Kahniashvili, A. G. Tevzadze, A. Brandenburg, and A. Neronov, *Phys. Rev. D* **87**, 083007 (2013).
- [59] A. Neronov, A. Roper Pol, C. Caprini, and D. Semikoz, *Physical Review D* **103** (2021), 10.1103/physrevd.103.1041302.
- [60] R. Durrer and A. Neronov, *The Astronomy and Astrophysics Review* **21** (2013), 10.1007/s00159-013-0062-7.



## Supplemental Material

**Discrete EOMs** To numerically solve Eq. 5 on the lattice, we adopt the standard staggered grid and leap-frog discretization. The scalar field and the gauge field are defined on alternating lattice sites,  $(n_0, \mathbf{n})$  and  $(n_0, \mathbf{n} + \frac{\mathbf{i}}{2})$ , respectively.

$$\begin{aligned} A_i(x, t) &\rightarrow (n_0, \mathbf{n} + \frac{\mathbf{i}}{2}), \quad \phi(x, t) \rightarrow (n_0 + \frac{1}{2}, \mathbf{n}), \quad \phi'(x, t) = \partial_0^- \phi \rightarrow (n_0, \mathbf{n}) \\ B_i(x, t) &= \nabla^+ \times \mathbf{A} \rightarrow (n_0, \mathbf{n} + \frac{\mathbf{j}}{2} + \frac{\mathbf{k}}{2}), \quad E_i(x, t) = \partial_0^+ A_i \rightarrow (n_0 + \frac{1}{2}, \mathbf{n} + \frac{\mathbf{i}}{2}) \end{aligned} \quad (21)$$

where the finite-difference operators  $\partial_0^\pm$  and  $\nabla^\pm$  correspond forward and backward differences. This definition in the time direction is the same with leap-frog method.

To ensure that each update involves only quantities located at the same lattice site, we introduce suitable local averaging and interpolation schemes, leading to the discrete evolution equations for the scalar and gauge momenta given in

$$\begin{aligned} \phi'(\tau + \Delta\tau) &= \phi'(\tau) \frac{a^2(\tau)}{a^2(\tau + \Delta\tau)} + \frac{d\tau}{a^2(\tau + \Delta\tau)} \left[ a^2(\tau) \nabla^+ \nabla^- \phi(\tau) - a^4(\tau) \frac{\partial V(\phi)}{\partial \phi}(\tau) \right. \\ &\quad \left. - \frac{\alpha}{v} a^4(\tau) E_i^{(2)}(\tau) (B_i^{(4)}(\tau) + B_i^{(4)}(\tau + \Delta\tau)) \right] \end{aligned} \quad (22)$$

$$A'_i(\tau) = A'_i(\tau - \Delta\tau) + d\tau \cdot a^2(\tau) \left[ -\epsilon_{ijk} \partial_j^- B_k(\tau) + \frac{\alpha}{2v} \left( \phi'(\tau) B_i(\tau) + \phi'_{+i}(\tau) B_{i,+i}(\tau) \right) - \frac{\alpha}{4v} \epsilon_{ijk} (K_{jk} + K_{jk,+i}) \right] \quad (23)$$

where we define

$$\begin{aligned} B_i^{(4)}(x) &= \frac{1}{4} [B_i(x) + B_{i,+j}(x) + B_{i,+k}(x) + B_{i,+j+k}(x)] \rightarrow (n_0, \mathbf{n}) \\ E_i^{(2)}(x) &= \frac{1}{2} [E_i(x) + E_{i,+i}(x)] \rightarrow (n_0 + \frac{1}{2}, \mathbf{n}) \\ K_{jk} &= \partial_j^- \phi(\tau) E_{k,-j} + \partial_j^+ \phi(\tau) E_{k,+j}(\tau) \end{aligned} \quad (24)$$

The variety  $E_{i,+i}(x, \tau) = E_i(x + i, \tau)$ ,  $\phi_{+i}(x, \tau) = \phi(x + i, \tau)$ . In addition, the discrete Gauss constraint is

$$\partial_i^- A'_i(\tau + \Delta\tau) = \frac{\alpha}{2} \left[ \partial_i^- \phi(\tau + \Delta\tau) \epsilon_{ijk} \partial_j^+ A_{k,-i}^{(2)}(\tau) + \partial_i^+ \phi(\tau + \Delta\tau) \epsilon_{ijk} \partial_j^+ A_{k,+i}^{(2)}(\tau) \right] \quad (25)$$

where  $A_i^{(2)}(x) = \frac{1}{2} (A_i(x) + A_i(x + i))$ . Last we can get the field  $\phi, A_i$

$$\begin{aligned} \phi(\tau + \Delta\tau) &= \phi(\tau) + \Delta\tau \phi'(\tau + \Delta\tau) \\ A_i(\tau + \Delta\tau) &= A_i(\tau) + \Delta\tau A'_i(\tau) \end{aligned} \quad (26)$$

This construction provides a stable and energy-conserving integration scheme suitable for long-term lattice simulations [34].

**Initial condition** For the axion field, since the dimensionless axion field  $\theta = a/v$  corresponds to the phase of the PQ field and its initial value is determined by spontaneous symmetry breaking during the PQ phase transition, the initial value of  $\theta$  is set as a uniform random distribution between 0 and  $2\pi$ . A dimensionless momentum cutoff  $\tilde{k}_{cut} = 1$  is imposed on the field to make the correlation length of axion field is about  $\lambda_a \sim 0.1H^{-1}$ . For the gauge field, we first use Eq. 14 to assign the initial magnetic field and then get the corresponding gauge field  $A_i(x)$  and its conjugate momentum  $A'_i(x)$  by using the method mentioned in [57].

In the PMF defined by Eq. 14, we can vary the UV cutoff  $k_{UV}$  to change the magnetic field's correlation length. It is thus necessary to identify physically meaningful values of correlation length relevant to the primordial magnetic field at the QCD phase transition. We consider two possible origins for the primordial magnetic field: the QCD phase transition and inflation. The QCD-sourced magnetic field typically has a correlation length  $\lambda \sim 0.1H^{-1}$  [58, 59] and a spectral index  $n = 2$  [60]. For inflation-generated fields, the comoving correlation length can be stretched arbitrarily



large if the field originates early enough during inflation. In this case, there is no upper bound on the comoving correlation length. The lower bound corresponds to magnetic fields produced at the end of inflation. Although interactions with the plasma can increase the correlation length [60], the minimum comoving correlation length at the QCD phase transition remains much smaller than the lattice spacing  $dx$ . Therefore, inflation allows us to explore a wide range of correlation lengths, both above and below the Hubble scale, and study their effects on the field evolution. The spectral index in this case depends on the specific inflationary model [60]. Therefore we will use the initial magnetic field with different correlation length and fix the spectrum index  $n = 2$  to avoid its influence.

In addition to the correlation length, the strength of the magnetic field must also be specified. Big Bang nucleosynthesis (BBN) imposes an observational constraint on the ratio of magnetic field energy density to radiation energy density, requiring  $\frac{\rho_B}{\rho_c} < 10\%$  across all scales. Although cosmic microwave background (CMB) measurements provide a stricter bound, they apply only on large scales (greater than 1Mpc today), which are well beyond the scales resolved by our lattice. Thus, we adopt our setup to ensure the BBN constraint  $\frac{\rho_B}{\rho_c} < 10\%$  at the end of simulation.

**The helicity** With the total helicity  $H = \int dx^3 \mathbf{A} \cdot \mathbf{B}_c$ , we can get

$$\begin{aligned} \frac{dH}{d\tau} &= \int dx^3 \mathbf{E}_c \cdot \mathbf{B}_c + \int dx^3 \mathbf{A} \cdot \frac{d}{d\tau}(\nabla \times \mathbf{A}) \\ &= \int dx^3 \mathbf{E}_c \cdot \mathbf{B}_c + \int dx^3 \mathbf{E}_c \cdot (\nabla \times \mathbf{A}) - \int dx^3 \nabla \cdot (\mathbf{A} \cdot \mathbf{E}_c) \\ &= 2 \int dx^3 \mathbf{E}_c \cdot \mathbf{B}_c \end{aligned} \quad (27)$$

where we have used the vanished integral on the boundary. This shows the non-zero oscillation of helicity gives the non-zero average Chern-Simons term  $F_{\mu\nu} \tilde{F}^{\mu\nu} = \mathbf{E} \cdot \mathbf{B}$ .

For the initial magnetic field defined in Eq. 14, the parameter  $\sigma_M$  determines the magnitude of magnetic helicity. We derive this relationship in detail below. In momentum space, we introduce the transverse orthogonal basis vectors

$$\hat{k} \cdot \hat{e}_\pm = 0, \quad \hat{e}_+ \cdot \hat{e}_- = 0, \quad i\hat{k} \times \hat{e}_\pm = \mp \hat{e}_\pm \quad (28)$$

The magnetic field can then be decomposed as  $\mathbf{B}(\mathbf{k}) = B^+(\mathbf{k})\hat{e}_+ + B^-(\mathbf{k})\hat{e}_-$ . The corresponding helicity and energy density in momentum space are given by

$$h(\mathbf{k}) = \mathbf{A}(\mathbf{k}) \cdot \mathbf{B}(\mathbf{k})^* = \frac{1}{k}(|B^+(\mathbf{k})|^2 - |B^-(\mathbf{k})|^2), \quad \rho_B(\mathbf{k}) = \frac{1}{2}\mathbf{B}(\mathbf{k}) \cdot \mathbf{B}(\mathbf{k})^* = \frac{1}{2}(|B^+(\mathbf{k})|^2 + |B^-(\mathbf{k})|^2) \quad (29)$$

The total helicity fraction is therefore

$$f_H = \frac{\sum_k h(k)}{\sum_k \frac{2\rho_B(k)}{k}} \in [-1, 1] \quad (30)$$

We further define the transverse and antisymmetric projection operators as

$$P_{ij}^T = \delta_{ij} - \hat{k}_i \hat{k}_j, \quad P_{ij}^A = \epsilon_{ijl} \hat{k}_l \quad (31)$$

With these operators, the initial magnetic field can be expressed as  $B_i(\mathbf{k}) = B_{ini} \Theta(k - k_{UV})(P_{ij}^T - i\sigma_M P_{ij}^A)g_j(\mathbf{k})k^n$ . Noting that  $P^\pm = \frac{1}{2}(P^T \mp iP^A)$  are the projection operators onto the  $\hat{e}_\pm$  basis, the field components can be written as

$$B_i^\pm(\mathbf{k}) = B_{ini} \Theta(k - k_{UV})(1 \pm \sigma_M)P_{ij}^\pm g_j(\mathbf{k}) = B_{ini} \Theta(k - k_{UV})(1 \pm \sigma_M)g_i^\pm(\mathbf{k}) \quad (32)$$

where  $g_i^\pm = P_{ij}^\pm g_j$  are the components of a Gaussian random field projected onto  $\hat{e}_\pm$ . Since  $g_j$  is statistically isotropic and non-helical, we have  $\sum_k |g_i^+(k)|^2 = \sum_k |g_i^-(k)|^2$ . Substituting these relations into Eq. 30, we obtain the final relation between  $f_H$  and  $\sigma_M$ : Last we have

$$f_H = \frac{\sum_k h(k)}{\sum_k \frac{2\rho_B(k)}{k}} = \frac{(1 + \sigma_M)^2 - (1 - \sigma_M)^2}{(1 + \sigma_M)^2 + (1 - \sigma_M)^2} = \frac{2\sigma_M}{1 + \sigma_M^2} \quad (33)$$

**The effective potential, average CS term and the decay parameter  $p$ .** As discussed in the text, the axion potential in Eq.2 is tilted by the CS coupling term  $\phi F_{\mu\nu} \tilde{F}^{\mu\nu}$ , as illustrated in the Fig.5. Here we use  $\langle F_{\mu\nu} \tilde{F}^{\mu\nu} \rangle \sim 10^{-6}$

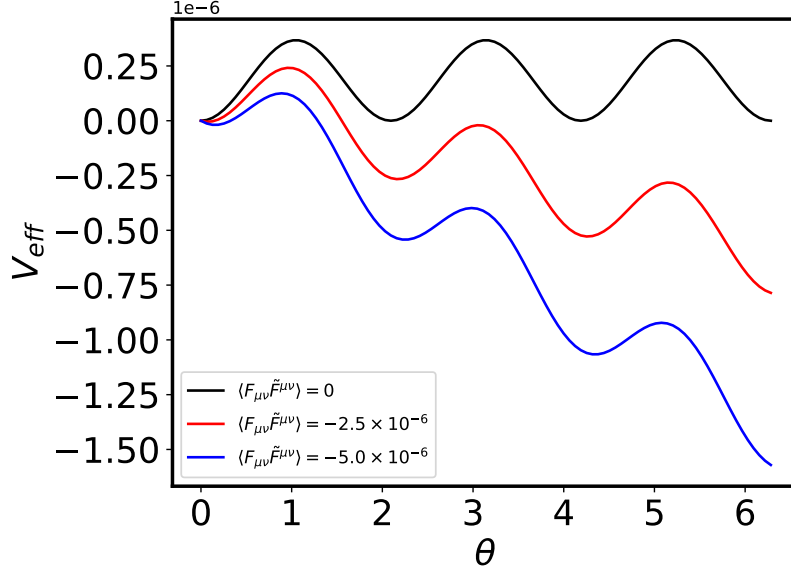


Figure 5: The effective potential defined by Eq. 9. We use different  $\langle F_{\mu\nu}\tilde{F}^{\mu\nu} \rangle$  to show the influence of CS term.

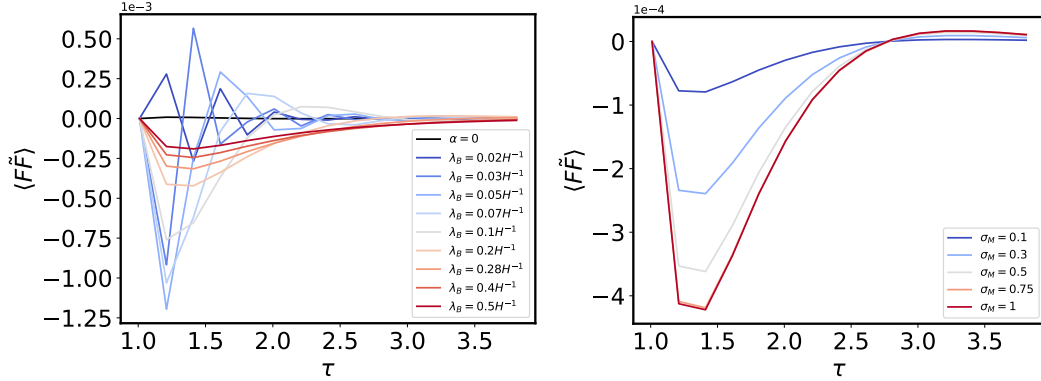


Figure 6: The evolution of average CS term. The left panel is cases with different  $\lambda_B$  and  $\sigma_M = 1$ . The right panel is cases with different  $\sigma_M$  and  $\lambda_B \sim 0.2H_i^{-1}$ .

to demonstrate the influence of the CS term, which is only about  $10^{-2}$  of the simulated average CS term shown in the Fig. 6. This indicates that, at the very beginning of the simulation, the CS coupling term dominates the field evolution. Such dominance is reasonable, since the average CS term  $\langle F_{\mu\nu}\tilde{F}^{\mu\nu} \rangle$  remains significant only for a very short period ( $1 < \tau < 2$ ), and a sufficiently large driving force is required to impart a non-negligible average velocity to the axion field.

We show the evolution of the average CS term at early times in the simulation in Fig. 6. The left panel presents results for different  $\lambda_B$  with fixed  $\sigma_M = 1$ , while the right panel shows results for different  $\sigma_M$  with fixed  $\lambda_B \sim 0.2H_i^{-1}$ . It is evident that the CS term oscillates rapidly for short correlation lengths and decreases as the correlation length increases. This behavior determines the net velocity of the axion field and, consequently, the decay rate of the DW network, as discussed in the main text. Furthermore, for a fixed correlation length, a decrease in  $\sigma_M$  reduces the CS term, which in turn slows down the decay of the DW network. Since the CS term decreases as  $a^{-4}$ , we only plot its evolution during the very early stages.

Finally, we use Eq.16 to show the evolution of the parameter  $p$  in Fig.7. The left panel presents results for different  $\lambda_B$  with fixed  $\sigma_M = 1$ , while the right panel shows results for different  $\sigma_M$  with fixed  $\lambda_B \sim 0.2H_i^{-1}$ . It is evident that  $p$  increases linearly with time in all cases, and the dotted line represents the corresponding fitting function. Using this fitting function, we can determine the time at which  $\mathcal{A}$  decreases to  $10^{-2}$  or  $10^{-1}$  of its value at the time of DW network formation, which defines the decay time.

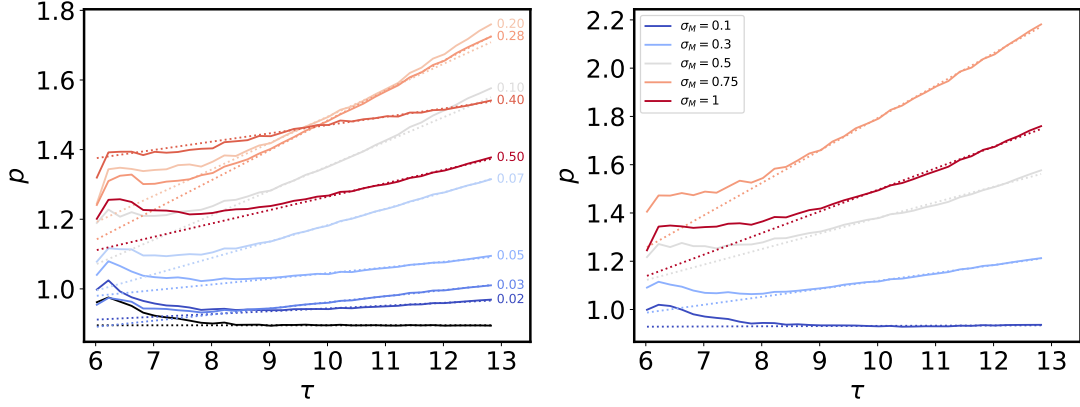


Figure 7: The evolution of  $p$ . The left panel is cases with different  $\lambda_B$  and  $\sigma_M = 1$ , where the value at the tail of each curve indicates the corresponding  $\lambda_B H_i$  associated with that case. The black curve corresponds the case  $\alpha = 0$ . The right panel is cases with different  $\sigma_M$  and  $\lambda_B \sim 0.2H_i^{-1}$ . The dotted line is the linear fitting function.

**The energy density of GW** As discussed in the text, the peak value of GW spectra can be parameterized as  $\Omega_{gw}^p \propto H^{-2} f_a^4 m_a^2$ .

$$\Omega_{gw}^p(t) = \tilde{\Omega}_1 \frac{f_a^4 m_a^2}{H(t)^2} \sim \tilde{\Omega}_2 \left( \frac{t_{\text{dec}}}{t_{\text{form}}} \right)^2 \left( \frac{f_a}{1.8 \times 10^{16} \text{GeV}} \right)^4 \quad (34)$$

where we have used  $H \sim m_a$  when the DW network forms and  $H = 1/(2t)$  in the radiation-dominate Universe. This equation is parameterized by our parameter values  $f_a = 1.8 \times 10^{16} \text{GeV}$ .

Consider the conservation of entropy give the evolution of temperature of Universe  $T \propto g_*(T)^{-1/3} a^{-1}$  and the GW energy density redshifts as  $\rho_{gw} \propto a^{-4}$ , we can get the GW spectra at the present day

$$\Omega_{gw,0}^p = \tilde{\Omega} \left( \frac{t_{\text{dec}}}{t_{\text{form}}} \right)^2 \left( \frac{f_a}{1.8 \times 10^{16} \text{GeV}} \right)^4 \left( \frac{10.75}{g_*(T_{\text{dec}})} \right)^{4/3} \quad (35)$$

Then we show the evolution of the GW energy density for each case in Fig. 8. In the case without coupling, the GW energy density approaches a constant value, indicating the onset of the scaling regime [32]. In contrast, when coupling to a fully helical magnetic field is included, the GW energy density decreases as the DW network decays.

**The DW-radiated axion energy density** We focus exclusively on the gauge-coupling cases. From the results in Fig 7, the parameter  $p$  is not constant and we can not get a simple analytical results as [19]. Therefore, we need some assumptions to simplify the computation.

Owing to the rapid decay of the DW network, we assume that its energy density remains approximately the same between the time of formation and the time of collapse. We further assume that, upon collapse, the entire energy stored in the DW network is instantaneously converted into free axion.

The total energy density of free axion

$$\rho_a \sim \rho_{dw,\text{form}} = \frac{\mathcal{A}_{\text{form}} \sigma_{dw}}{t_{\text{form}}} = 2\mathcal{A}_{\text{form}} \sigma_{dw} \left( \frac{t_{\text{dec}}}{t_{\text{form}}} \right) H_d \quad (36)$$

Using conservation of entropy  $s = \frac{2\pi^2}{45} g_*(T) T^3 \propto a^{-3}$ , we can get the axion energy density after DW network collapsing

$$\rho_a(t) = m_a(0) n_a(t_{\text{dec}}) \left( \frac{a(t_{\text{dec}})}{a(t)} \right)^3 = 2\epsilon_a \mathcal{A}_{\text{form}} \sigma_{dw} \left( \frac{t_{\text{dec}}}{t_{\text{form}}} \right) H_d \left( \frac{s(t)}{s(t_{\text{dec}})} \right) \quad (37)$$

Using  $T_d \propto \sqrt{H_d M_{pl}}$  and considering the radiation-matter equality  $\rho_{DM} = \rho_r = \frac{\pi^2}{30} g_*(T_{eq}) T_{eq}^4$ , we can get the ratio

$$\frac{\Omega_a}{\Omega_{DM}} \sim \frac{\epsilon_a \mathcal{A}_{\text{form}} \beta f_a^2 m_a}{T_{eq} H_d^{1/2} M_{pl}^{3/2}} \left( \frac{t_{\text{dec}}}{t_{\text{form}}} \right) \sim \frac{\epsilon_a \mathcal{A}_{\text{form}} \beta f_a^2 m_a^{1/2}}{T_{eq} M_{pl}^{3/2}} \left( \frac{t_{\text{dec}}}{t_{\text{form}}} \right)^{3/2} \quad (38)$$

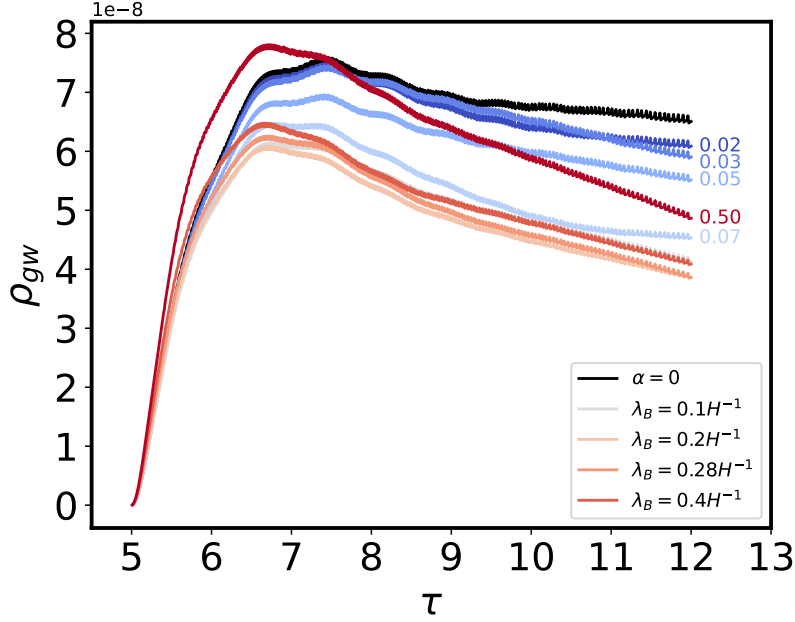


Figure 8: This figure gives the evolution of GW energy density. The values at the tail of each curve indicates the corresponding  $\lambda_B H_i$  associated with that case. The black curve corresponds the case  $\alpha = 0$ . The curves for some cases is so close that we can not put the  $\lambda_B H_i$  at the tail, so we use the legend to show there correlation length.

where we have used  $H \sim m_a$  when the DW network forms and  $H = 1/(2t)$ . The parameter  $\beta$  is defined as  $\beta = \sigma_{dw}/(m_a f_a^2) = 9.32$  and  $\epsilon_a = \bar{k}_a/m_a$ .

Substitute the constant coefficient, we can get

$$\begin{aligned} \frac{\Omega_a}{\Omega_{DM}} &\sim 5 \times 10^5 \epsilon_a \mathcal{A}_{\text{form}} \left( \frac{t_{\text{dec}}}{t_{\text{form}}} \right)^{3/2} \left( \frac{f_a}{1.8 \times 10^{16} \text{GeV}} \right)^2 \left( \frac{m_a}{3.2 \times 10^{-10} \text{eV}} \right)^{1/2} \left( \frac{10.75}{g_*(T_{\text{dec}})} \right)^{1/4} \\ &\sim 0.085 \epsilon_a \mathcal{A}_{\text{form}} \left( \frac{t_{\text{dec}}}{t_{\text{form}}} \right)^{3/2} \left( \frac{f_a}{10^{12} \text{GeV}} \right)^2 \left( \frac{m_a}{10^{-6} \text{eV}} \right)^{1/2} \left( \frac{10.75}{g_*(T_{\text{dec}})} \right)^{1/4} \end{aligned} \quad (39)$$

The first row is normalized by simulation parameters  $f_a = 1.8 \times 10^{16} \text{GeV}$ ,  $m_a = 3.2 \times 10^{-10} \text{eV}$ . The extremely large coefficient  $3.6 \times 10^5$  shows these parameters is so large that the axion is over-produced. The last row is normalized by the parameters shown in [38]  $f_a \sim 10^{12} \text{GeV}$ ,  $m_a \sim 10^{-6} \text{eV}$ .

The above calculation requires the average momentum parameter  $\epsilon_a$ , which can be obtained from the spectrum of the axion energy density. We plot the evolution of  $\epsilon_a$  in the left panel of Fig. 9 and the right panel shows the spectrum radiated at  $\tau = 11$ . In the spectra figure, we remove the unphysical high-frequency component by subtracting the initial spectrum. The spectra are all peaked in the high-frequency region and it is larger for the long-correlation cases, which is consistent with the results of  $\epsilon_a$ .

**The results of  $t_{\text{dec}}$ ,  $\mathcal{A}_{\text{form}}$ ,  $\epsilon_a$  and  $\tilde{\Omega}$  and fitting functions.** We first present the parameters  $\log_{10}(\frac{t_{\text{dec}}}{t_{\text{form}}})$ ,  $\mathcal{A}_{\text{form}}$ ,  $\epsilon_a$  and  $\tilde{\Omega}$  for different  $\lambda_B$  with fixed  $\sigma_M = 1$  in Fig.10. All of these parameters can be fitted using piecewise linear or linear functions, which reflects the differing influences of long and short correlation lengths, as discussed in the main text. Using these results and the corresponding fitting functions, we can obtain the expressions in Eq.17 and Eq. 20.

In addition, we show the results of these parameters for different values of  $\sigma_M$  with  $\lambda_B \sim 0.2 H_i^{-1}$  in Fig. 11. The ratio  $\log_{10}(\frac{t_{\text{dec}}}{t_{\text{form}}})$  is proportional to  $1/f_H$  and the scaling parameter at the formation of the DW network,  $\mathcal{A}_{\text{form}}$ , is also well fitted by  $\mathcal{A}_{\text{form}} \propto 1/f_H$ , which is consistent with the interpretation that faster-decaying DW networks form with smaller areas. The average momentum parameter  $\epsilon_a$  follows  $\epsilon_a \propto f_H$ , indicating that faster decay produces higher-frequency axions for the same  $\lambda_B$ . Finally, the peak amplitude of the GW spectrum,  $\Omega_{gw,0}^p h^2$ , satisfies  $\Omega_{gw,0}^p h^2 \propto 1/f_H$ , in agreement with the fact that rapidly decaying DW networks emit less GW energy.

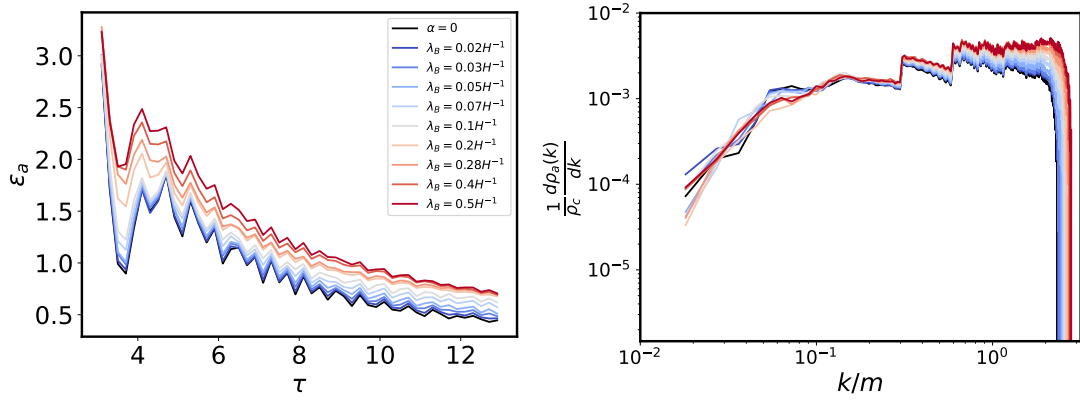


Figure 9: The average momentum parameter  $\epsilon_a$  and axion energy density spectra at  $\tau = 11$ . In the right panel, the correspondence between color and  $\lambda_B$  is the same as the legend in the left panel.

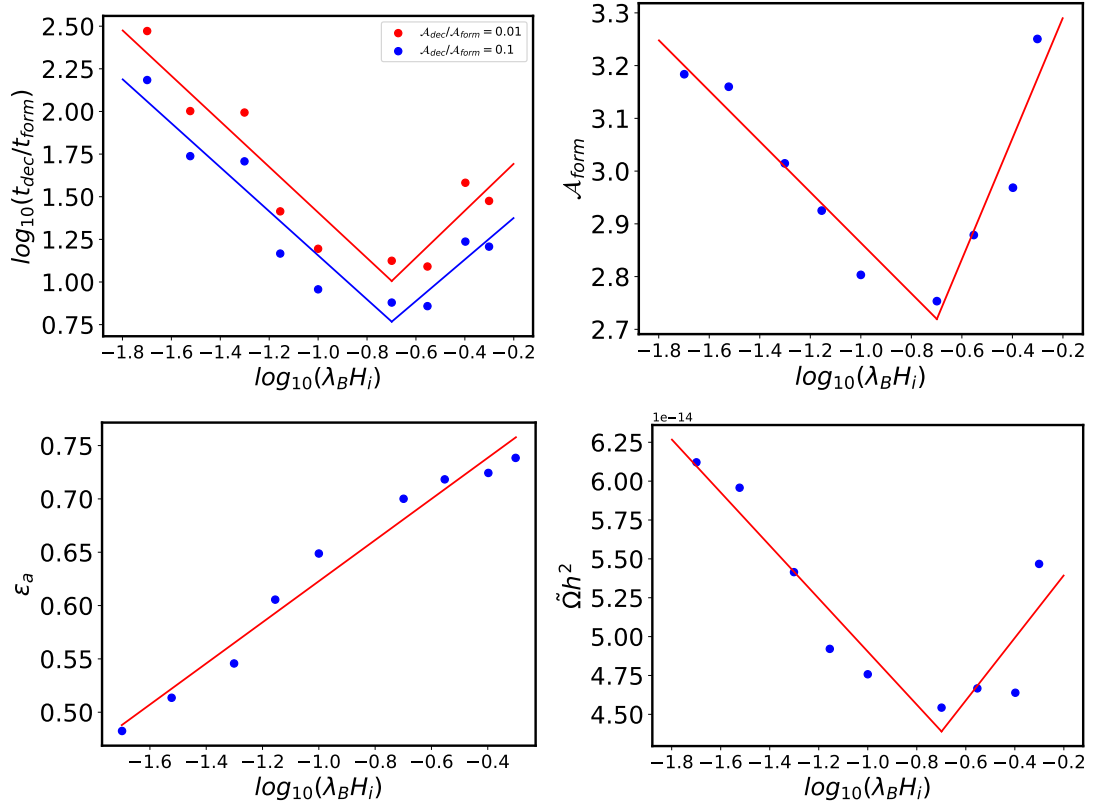


Figure 10: These results are all from the case  $\sigma = 1$  for different  $\lambda_B$ . The red curve is the fitting function.

We now present the efficiency parameter of GW radiation. Rewriting the  $\Omega_{gw}$  as

$$\Omega_{gw} = \frac{\rho_{gw}}{\rho_c} = \epsilon_{gw} \frac{8\pi G^2 \sigma_{gw}^2}{3H^2} = \epsilon_{gw} \beta^2 \frac{8\pi G^2 m_a^2 f_a^4}{3H^2} \quad (40)$$

where we define  $\epsilon_{gw} = \rho_{gw}/(G\sigma_{dw}^2)$  is the efficiency parameter. With the results of  $\Omega_{gw}^p$  then we can get the  $\epsilon_{gw}$  for each cases in Fig 12

For the above factors  $\epsilon_a, \mathcal{A}_{form}, \tilde{\Omega}$  and the factor in the text  $t_{dec}/t_{form}$ , we have derived the relation to  $\lambda_B$ , now we consider their relation with the magnitude of coupling term  $C = \alpha F_{\mu\nu} \tilde{F}^{\mu\nu}$ . Through the analysis in the text, we can parameterize this term

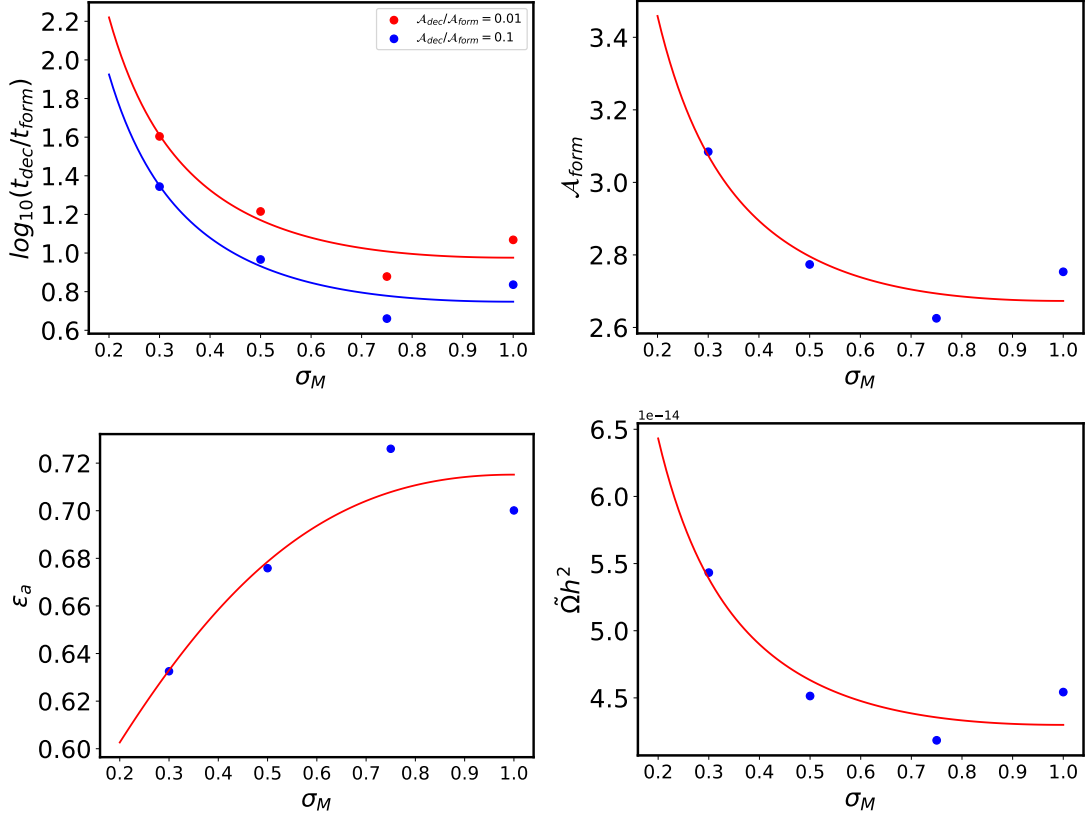


Figure 11: These results are all from the case  $\lambda_B \sim 0.2H_i^{-1}$  and different  $\sigma_M$ . The red curve is the fitting function.

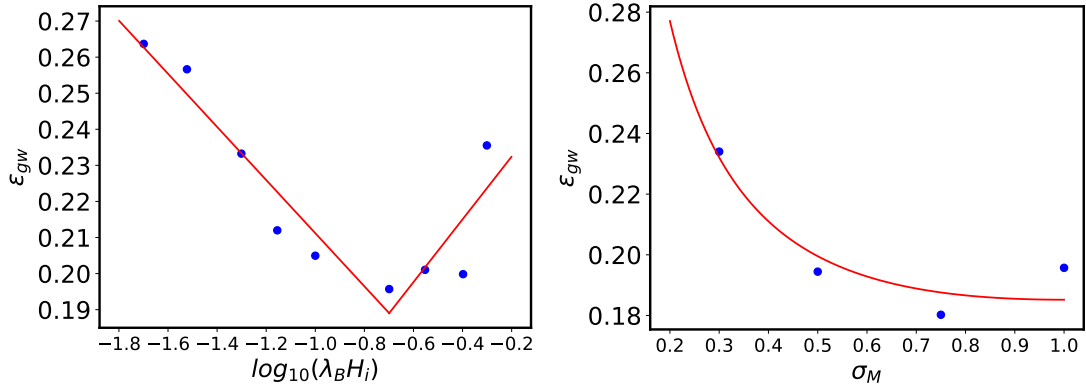


Figure 12: The efficiency parameter of GW radiation. Left: The cases for different  $\lambda_B$  and fixed  $\sigma_M = 1$ . Right: The cases for different  $\sigma_M$  and fixed  $\lambda_B \sim 0.2H_i^{-1}$ .

For the quantities  $\epsilon_a$ ,  $\mathcal{A}_{\text{form}}$ ,  $\tilde{\Omega}$ , and the decay-time ratio  $t_{\text{dec}}/t_{\text{form}}$ , we have already derived their dependence on the PMF correlation length  $\lambda_B$ . We now extend this analysis to determine how these quantities scale with the magnitude of the gauge–axion coupling term,  $C = \alpha F_{\mu\nu} \tilde{F}^{\mu\nu}$ . Based on the discussion in the text, this coupling term can be parameterized as

$$C(\alpha, B_{\text{ini}}, f_H) = \left(\frac{\alpha}{\alpha_0}\right) \left(\frac{B_{\text{ini}}^2}{B_0^2}\right) \left(\frac{f_H}{f_{H,0}}\right) C_0 \quad (41)$$

where  $\alpha_0 = 0.2$ ,  $f_{H,0} = 1$  are the reference values adopted in our simulations. In these simulations, we varied  $f_H$  while keeping  $\alpha = \alpha_0$ ,  $B_{\text{ini}} = B_0$  for  $\lambda_B \sim 0.2H_i^{-1}$  case and obtained the dependence of  $\epsilon_a$ ,  $\mathcal{A}_{\text{form}}$ ,  $\tilde{\Omega}$ , and  $t_{\text{dec}}/t_{\text{form}}$  on  $f_H$ .

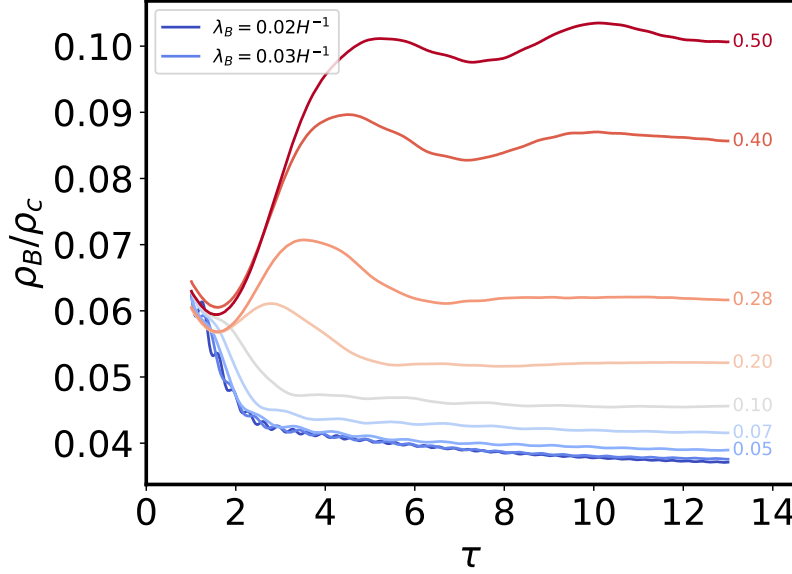


Figure 13: This figure shows the evolution of ratio  $\rho_B/\rho_c$  for each cases, where the value at the tail of each curve indicates the corresponding  $\lambda_B H_i$  associated with that case. The black curve corresponds the case  $\alpha = 0$ .

Taking  $\mathcal{A}_{\text{form}}$  as an example, we found  $\mathcal{A}_{\text{form}} \propto \frac{1}{f_H}$ . Since the physical quantity that governs the dynamics is the magnitude of the coupling term  $C$  rather than  $f_H$  alone, the above dependence can be rewritten as

$$\begin{aligned} \mathcal{A}_{\text{form}}(\alpha_0, B_0, f_H) &= \mathcal{A}_{\text{form}}(\alpha_0, B_0, f_{H,0}) + k_f \left( \frac{1}{f_H} - \frac{1}{f_{H,0}} \right) = \mathcal{A}_{\text{form}}(\alpha_0, B_0, f_{H,0}) + \frac{k_f}{f_{H,0}} \left( \frac{C_0}{C(\alpha_0, B_0, f_H)} - 1 \right) \\ \mathcal{A}_{\text{form}}(\alpha, B_0, f_{H,0}) &= \mathcal{A}_{\text{form}}(\alpha_0, B_0, f_{H,0}) + k_\alpha \left( \frac{1}{\alpha} - \frac{1}{\alpha_0} \right) = \mathcal{A}_{\text{form}}(\alpha_0, B_0, f_{H,0}) + \frac{k_\alpha}{\alpha_0} \left( \frac{C_0}{C(\alpha, B_0, f_{H,0})} - 1 \right) \end{aligned} \quad (42)$$

If we choose parameters satisfying  $f_{H,1}/f_{H,0} = \alpha_1/\alpha_0$ , then  $C(\alpha_0, B_0, f_{H,1}) = C(\alpha_1, B_0, f_{H,0})$ , which implies  $\mathcal{A}_{\text{form}}(\alpha_0, B_0, f_{H,1}) = \mathcal{A}_{\text{form}}(\alpha_1, B_0, f_{H,0})$ . This equality requires  $\frac{k_f}{f_{H,0}} = \frac{k_\alpha}{\alpha_0}$ . An analogous argument applies to variations in  $B_{\text{ini}}$ . Combining all contributions, the general dependence of  $\mathcal{A}_{\text{form}}$  on the couplings  $(\alpha, B_{\text{ini}}, f_H)$  can be expressed as

$$\mathcal{A}_{\text{form}}(\alpha, B_{\text{ini}}, f_H) = \mathcal{A}_{\text{form}}(\alpha_0, B_0, f_{H,0}) + k \left( \frac{\alpha_0}{\alpha} \frac{B_0^2}{B_{\text{ini}}^2} \frac{f_{H,0}}{f_H} - 1 \right) \quad (43)$$

where  $k = k_f/f_{H,0}$  is determined from simulation. The same procedure applies to the other parameters  $\epsilon_a, \tilde{\Omega}$  and  $t_{\text{dec}}/t_{\text{form}}$ . In our analysis, we assume that the slope  $k$  remains approximately independent of the correlation length  $\lambda_B$ .

**The backreaction of magnetic energy density** We now consider the evolution of magnetic field energy density, which can show the backreaction of the gauge-coupling. The ratio of the magnetic field energy density to the background radiation energy density  $\rho_B/\rho_c$  is plotted in Fig. 13. For the case without coupling  $\alpha = 0$ , this ratio decreases as the number of relativistic degrees of freedom  $g_*(T)$  decreases. When  $\alpha \neq 0$ , the coupling transfers energy from the axion field to the gauge field, causing the magnetic field energy density to increase. From this figure, we also find that the energy growth is larger for magnetic fields with longer correlation lengths. The initial strength of the magnetic field is chosen such that the ratio satisfies the BBN constraint.

**The 3D distribution of DW network** We plot the distribution of the DW network for each case at the same time in Fig. 14. These figures provide an intuitive illustration of the decay behavior of DW networks coupled to helical PMFs and show the different decay rates for different PMF correlation lengths.



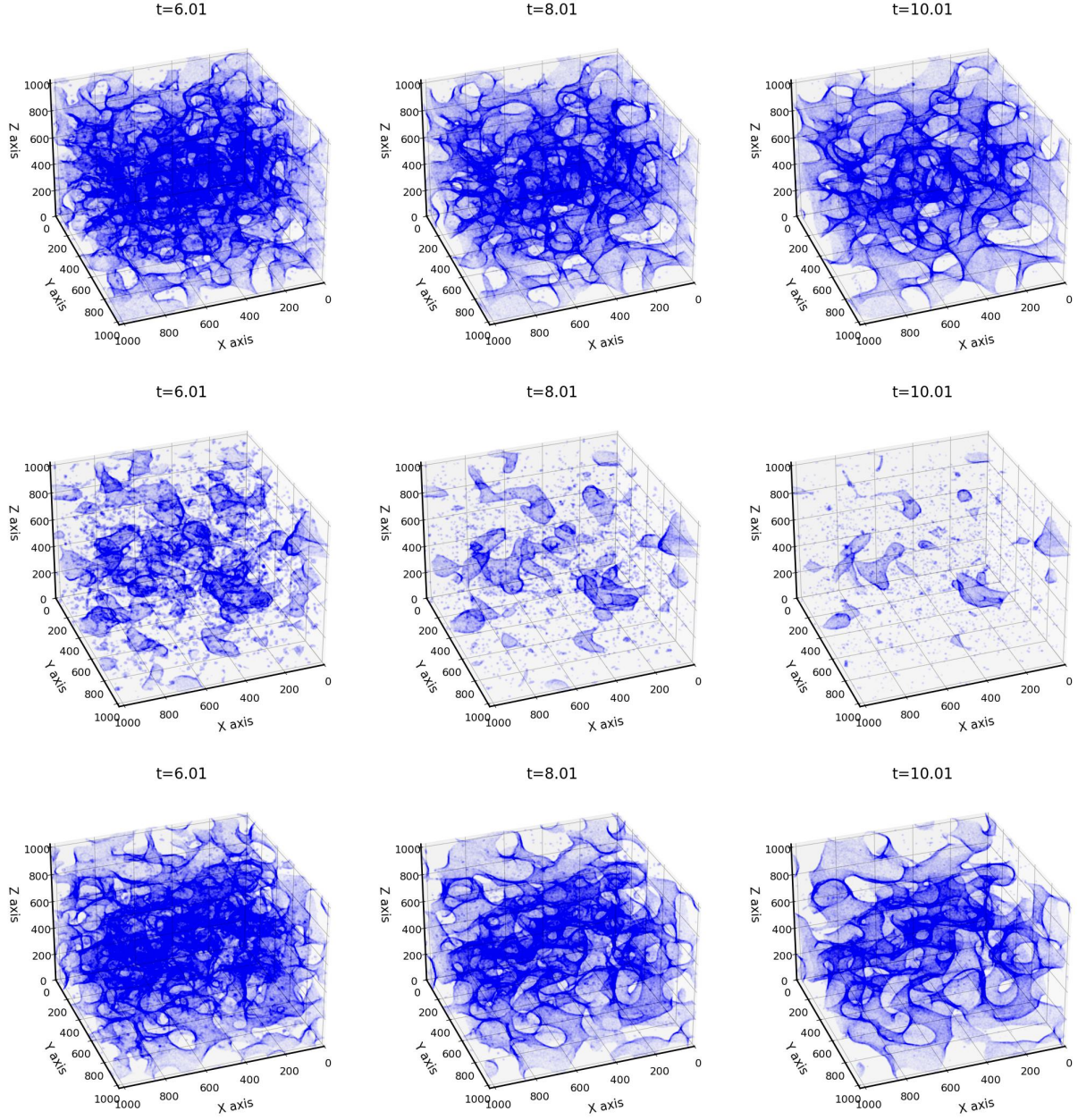


Figure 14: The distribution of DW network at time  $\tau = 6.01$ ,  $\tau = 8.01$  and  $\tau = 10.01$ . From top to bottom, the figures show the results of case  $\alpha = 0$ ,  $\lambda_B = 0.1H^{-1}$  and  $\lambda_B = 0.02H^{-1}$ .